JGR Atmospheres

RESEARCH ARTICLE
10.1029/2020JD033085

Global Wildfire Plume-Rise Data Set and Parameterizations for Climate Model Applications

Ziming Ke[1], Yuhang Wang[1], Yufei Zou[1], Yongjia Song[1], and Yongqiang Liu[2]

[1]School of Earth and Atmospheric Science, Georgia Institute of Technology, Atlanta, GA, USA, [2]Center for Forest Disturbance Science, Southern Research Station, U.S. Department of Agriculture Forest Service, Athens, GA, USA

Key Points:

- An observation-based fire plume height data set is developed for 2002–2010. It is in general agreement with global Multiangle Imaging SpectroRadiomete observations
- Late morning satellite observations tend to underestimate the fraction of fire plumes reaching the free troposphere during the day
- Modeling using online fire plume-rise parameterizations based on this data set shows extensive free-tropospheric transport of fire aerosols

Supporting Information:

- Supporting Information S1
- Supporting Information S2
- Supporting Information S3

Correspondence to:

Y. Wang,
yuhang.wang@eas.gatech.edu

Citation:

Ke, Z., Wang, Y., Zou, Y., Song, Y., & Liu, Y. (2021). Global wildfire plume-rise data set and parameterizations for climate model applications. *Journal of Geophysical Research: Atmospheres*, *126*, e2020JD033085. https://doi.org/10.1029/2020JD033085

Received 17 MAY 2020
Accepted 18 FEB 2021

Author Contributions:

Conceptualization: Ziming Ke, Yuhang Wang
Data curation: Ziming Ke, Yongjia Song
Formal analysis: Ziming Ke
Funding acquisition: Yuhang Wang
Investigation: Ziming Ke
Methodology: Ziming Ke, Yuhang Wang, Yufei Zou
Project Administration: Yuhang Wang
Resources: Ziming Ke, Yuhang Wang, Yufei Zou
Software: Ziming Ke, Yufei Zou, Yongjia Song
Supervision: Yuhang Wang, Yongqiang Liu

Abstract The fire plume height (smoke injection height) is an important parameter for calculating the transport and lifetime of smoke particles, which can significantly affect regional and global air quality and atmospheric radiation budget. To develop an observation-based global fire plume-rise data set, a modified one-dimensional plume-rise model was used with observation-based fire size and Maximum Fire Radiative Power (MFRP) data, which are derived from satellite fire hotspot measurements. The resulting data set captured well the observed plume height distribution derived from the Multiangle Imaging SpectroRadiometer (MISR) measurements. The fraction of fire plumes penetrating above the boundary layer is relatively low at 20% at the time of MISR observation (10:30 am LT) but increases to an average of ~55% in the late afternoon, implying that the MISR observation data sampled in late morning underestimate the average daytime fire plume heights and plume mixing into the free troposphere. Therefore, adjustments are required through dynamic modeling or parameterization of fire plume height as a function of meteorological and fire conditions when the MISR data set is applied in climate model simulations. We conducted sensitivity simulations using the Community Atmospheric Models version 5 (CAM5). Model results show that the incorporation of fire plume rise in the model tends to significantly increase fire aerosol impacted regions. We applied the offline plume-rise data to develop an online fire plume height parameterization, allowing for simulating the feedbacks of climate/weather on fire plume rise in climate models.

Plain Language Summary The wildfire smoke injection height is important to study the lifetime and transport capacity of smoke particles. This study developed a long-term global wildfire injection height data set, which has been well evaluated and applied to global climate model simulation. For fully coupled atmosphere-land simulation purposes, implementation has been developed for the climate model to generate injection height at each time step. The fire plume height (smoke injection height) is important for calculating the transport and lifetime of smoke particles. A modified one-dimensional plume-rise model was used with observation-based fire size and Maximum Fire Radiative Power (MFRP) data. The resulting data set captured well the observed plume height distribution. The simulated plume penetration rate suggests higher fire emission mixed in the free troposphere in the late afternoon. We conducted sensitivity simulations using the Community Atmospheric Models version 5 (CAM5). In downwind regions, model results show that the incorporation of fire plume rise tends to increase fire aerosol transport. Additionally, we develop an online fire plume height parameterization, allowing for simulating the feedbacks of climate/weather on fire plume rise in climate models.

1. Introduction

Wildfires release large amounts of greenhouse gases, carbonaceous aerosols, and other pollutants, therefore having complex impacts on climate, local weather, and air quality. CO_2 released from fires (2–4 Pg C yr^{-1}) is up to half of that from fossil-fuel combustion (7 Pg C yr^{-1}) (e.g., Browman et al., 2009; van der Werf et al., 2006). In addition to greenhouse gases, carbonaceous aerosols (organic and black carbon) released from fires modulate atmospheric radiative balance directly through scattering and absorbing solar radiation and indirectly through changing cloud properties (e.g., Bauer & Menon, 2012; Boucher et al., 2013; Jiang et al., 2016). Climate model experiments indicated that organic carbonaceous aerosols generally increase the aerosol optical depth (AOD) and reduce surface temperature, while black carbon aerosols enhance heat absorption in the troposphere, leading to warming in the free troposphere and cooling at the surface; the resulting atmospheric stability changes could potentially suppress atmospheric convection and subsequently

Validation: Ziming Ke
Visualization: Ziming Ke
Writing – original draft: Ziming Ke, Yuhang Wang
Writing – review & editing: Ziming Ke, Yuhang Wang, Yufei Zou, Yongqiang Liu

affect atmospheric circulations (e.g., Bauer & Menon, 2012; Liu, 2005a, 2005b; Tosca et al., 2013). In the tropics, previous studies highlighted the role of black carbon in changing the Hadley circulation and precipitation patterns (Allen et al., 2012; Hodnebrog et al., 2016; Tosca et al., 2015). At the middle to high latitudes, previous studies indicated potential impacts of smoke emissions on regional climate and weather patterns (e.g., Grell et al., 2011; Liu, 2004; Madden et al., 2015), and severe weather evens (Saide et al., 2016). Additionally, evidence was found for the effects of high latitude wildfires on the Arctic air quality during spring and summer (Evangeliou et al., 2016; Monks et al., 2012; Winiger et al., 2016) and for potential impacts on Greenland ice shelves melting (Keegan et al., 2014).

To accurately simulate the impacts of wildfire emissions, a crucial parameter is fire plume height or injection height, defined as the highest altitude in the atmosphere the smoke can reach. This parameter affects the transport of smoke particles and thereby influences climate and air quality in the downwind regions. Generally, if the plume heights are above the Atmospheric Boundary Layer (ABL), the smoke particles can be transported far away from a fire site because of higher wind speed in the free troposphere than the ABL. In contrast, the impacts of smoke particles within the ABL are restricted to smaller regions (e.g., Liu et al., 2014; Paugam et al., 2016; Vernon et al., 2018).

The reported fire plume heights range from entirely within the ABL (Trentmann et al., 2002), to the free troposphere (de Gouw et al., 2006), even the stratosphere (Dirksen et al., 2009; Ditas et al., 2018; Yu et al., 2019). The fire plume heights derived from the Multiangle Imaging SpectroRadiometer (MISR) stereo imaging developed by Kahn et al. (2007) were widely used to evaluate model simulated plume height data (e.g., Kahn et al., 2008; Tosca et al., 2011; Val Martin et al., 2010) with a resolution of 500 m in the vertical and 1.1 km in the horizontal (Kahn et al., 2007). The vertical resolution improved to 250 m in the recent update (Val Martin et al., 2018). The global MISR wildfire plume height data set is available at https://www-misr.jpl.nasa.gov/getData/accessData/MisrMinxPlumes/.

An interesting result of the MISR fire plume height data is that the fraction of fire plume height above the ABL is relatively low, ~10% over North America (Kahn et al., 2008; Val Martin et al., 2010) and only 4% in Southeast Asia (Tosca et al., 2011). However, the MISR instrument is onboard the sun-synchronous Terra satellite; its local equatorial crossing time is approximately 10:30 a.m. Hence, MISR data only represented fire plume heights in the late morning and likely missed the daily maximum fire plume heights that would occur in the late afternoon due to the diurnal variation of wildfires intensity (Ellicott et al., 2009) and unstable ABL conditions (Sofiev et al., 2012). Therefore, a fire plume height data set that captures the diurnal variation on a global scale is needed in order to improve the understanding of the temporal and spatial variability of fire plume heights and their impacts. In the same vein, a dynamic model or online parameterization is required to simulate the feedbacks of climate/weather on fire intensity and atmospheric stability and their effects on fire plume rise in climate models.

Val Martin et al. (2012) applied 1-D plume-rise model, which is a physics-based dynamic model developed by Freitas et al. (2007, 2010), with Moderate Resolution Imaging SpectroRadiometer (MODIS) Fire Radiative Power (FRP) and assimilated GEOS meteorology data to calculate the wildfire plume heights over North America for the 2002 and 2004–2007 fire seasons, and compared the results with the MISR plume heights. They suggested that the plume-rise model tends to underestimate when the observed plume heights are high, but they did not investigate the diurnal variation of wildfire plume heights. The relatively coarse spatial ($2° \times 2.5°$) and temporal (± 3 h) resolutions of meteorological data may have contributed to the estimated model biases due to the sensitivity of wildfire plume height to ambient meteorological conditions (Sofiev et al., 2012).

In this work, we attempt to develop a global hourly smoke plume height data set based on observations, and formulate a corresponding online parameterization to use in climate model applications based on the 1-D plume-rise model by Freitas et al. (2007, 2010). Using assimilated high-resolution meteorological reanalysis and satellite observations, we improved upon previous studies to develop an observation-based (offline) global fire plume height data set from 2002 to 2010 that account for diurnal variability in wildfire intensity and meteorological data. This data set is then applied to formulate an online parameterization of fire plume height for use in climate model simulations. The observation and assimilated meteorological data, modifications and application of the 1-D dynamic fire plume height model, the online parameterization of fire

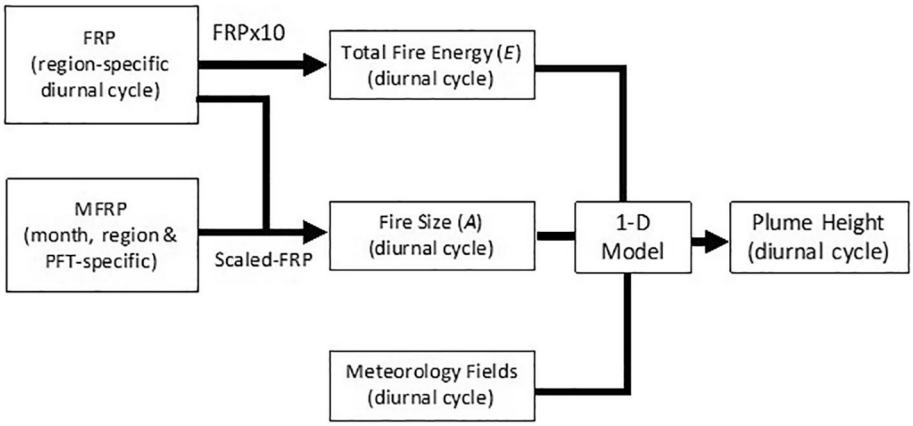

Figure 1. The schematic diagram for calculating the offline fire plume height data set.

plume height, and climate simulations are described in Section 2. The evaluation of the global fire plume height data set with observations and climate model simulations and assessments using the prescribed global fire plume height data set or the online fire plume height parameterization are discussed in Section 3. Conclusions are given in Section 4.

2. Data, Models, and Methods

2.1. Offline Global Fire Plume Height Calculation and Evaluation

In this study, we calculated hourly global smoke plume heights from 2002 to 2010 based on available observation data. The input data for simulating smoke plume rise using the 1-D model by Freitas et al. (2007, 2010) are illustrated in Figure 1. To improve the accuracy of the calculations, we made use of satellite observations and assimilated meteorological data to provide the model input data. We describe the methods for data processing in the following sections: including (1) meteorological data, fire region, and plant function type (PFT), (2) computing the total fire energy and the fire size data, (3) the 1-D fire plume-rise model modifications, and (4) fire plume height diurnal variation. We then describe the MISR fire plume height and MODIS AOD data for model evaluations.

2.1.1. Meteorology Data, Fire Regions, and Plant Functional Types

The meteorology fields from 2002 to 2010 were obtained from the Climate Forecast System Reanalysis (CFSR) hourly forecast data, with a $0.5° \times 0.5°$ horizontal resolution and 37 vertical layers (Saha et al., 2014). We used four meteorology variables, the temperature, geopotential height, specific humidity, and wind, from land surface to the top of troposphere. The hourly and high spatial resolution assimilated CSFR meteorological data are needed for the calculation of the fire plume height due to the high sensitivity of fire plume rise to atmospheric conditions (Sofiev et al., 2012).

To further improve the 1-D fire plume modeling, we derived fire characteristics (next section and Figure 1) as a function of regions and PFT types. Fifteen wildfire regions were used in this study (Figure S1 and Table S1), same as the 14 Global Fire Emissions Database (GFED) regions (Giglio et al., 2013) except that the GFED Temperate North America was split into two regions of western (WTNA) and eastern (ETNA) to considering more prevalent prescribed burning in the eastern United State (Zeng et al., 2008). The effects of different vegetation within a region in wildfires were considered through PFT data, which were derived from MODIS Landcover data set MCD12Q1 (e.g., Channan et al., 2014). We used six PFT categories, including needle leaf forest, broadleaf forest, shrub, grass, crop, and unvegetated. These are simplified from the 16 MODIS landcover data set categories (Table S2). The spatial PFT distribution is shown in Figure S2.

2.1.2. Fire Size and Total Fire Energy Flux

We used the MODIS MCD14ML global monthly fire location products (Giglio, 2013) to compute the size of an observed fire. Following the approach by Val Martin et al. (2012), the fire size per grid cell (A_{gc} in km^2) was calculated

$$A_{gc} = \Delta r * \frac{FRP_{gc}}{MFRP}, \tag{1}$$

where Δr is the resolution of the detected fire (1 km^2 for MODIS MCD14ML data), and FRP_{gc} is the FRP of the fire grid cell. The *MFRP*, Maximum Fire Radiative Power, is defined as the 99th percentile value of all detected FRP_{gc} values for a given wildfire region, PFT type, and calendar month from 2001 to 2014. The *MFRP* is assumed to be the *FRP* value when the whole grid cell is burned and hence, $FRP_{gc}/MFRP$ represents the burned fraction of a grid cell. The values of MFRP are listed in Table S3. Adjacent nonzero FRP_{gc} grid cells are aggregated to be one fire (Kahn et al., 2007; Val Martin et al., 2010), i.e., the sums of A_{gc} and the products of FRP_{gc} and $\frac{FRP_{gc}}{MFRP}$ of these fire grid cells are the size and FRP of this fire, respectively.

Another fire parameter for the 1-D model is the total fire energy flux. Previous studies showed that the satellite detected fire radiative energy is about 10% of the total fire energy (Freeborn et al., 2008; Wooster et al., 2005). We followed the work by Val Martin et al. (2012) to compute the total fire energy flux of a fire (E)

$$E = 10 * FRP_{fire}, \tag{2}$$

where FRP_{fire} is the FRP value of an identified fire; the FRP unit is MW for a grid cell of 1 km^2, and we convert the unit to W/m^2.

2.1.3. 1-D Fire Plume-Rise Model Modifications

The meteorology and fire data described above were fed into the 1-D plume-rise model developed by Freitas et al. (2007, 2010) to compute an offline global smoke plume height data set (Figure 1). This physical fire plume-rise model scheme is governed by the conservations of energy, vertical momentum, and mass. It was previously implemented in regional air quality and climate models (e.g., Grell et al., 2011; Pfister et al., 2011; Stein et al., 2009). The prognostic equation of vertical momentum (Freitas et al., 2007) is

$$\frac{\partial w}{\partial t} + w\frac{\partial w}{\partial z} = \frac{1}{1+\gamma} gB - \frac{2\alpha}{R} w^2 + \frac{\partial}{\partial z}\left(K_{zz}\frac{\partial w}{\partial z}\right), \tag{3}$$

where w is the vertical velocity, t is the time, z is the vertical distance, g is the acceleration due to gravity, and γ is the parameter for nonhydrostatic pressure perturbations and was set to be 0.5 in this study (Simpson & Wiggert, 1969). The parameter, B, is the buoyance term related to the difference of temperature between fire plume air parcel and the ambient environment (see the supporting information ST1). The initial velocity and temperature difference between fire plume and ambient air (δT in Figure 2) are functions of fire size, MFRP, surface air temperature, and surface pressure (Freitas et al., 2007). The parameter, α, is the entrainment coefficient with a default value of 0.1. R is the radius of the plume air parcel. The eddy diffusion coefficient, K_{zz}, was assumed to be constant in the original model. Following the work by Myrup and Ranzieri (1976), we set the K_{zz} vertical profile as a parabolic function, increasing from the surface, reaching the peak in the middle of the boundary layer and decreasing to a small value at the top of boundary layer. The default K_{zz} value of 500 m^2 s^{-1} was used in the tropics and subtropics (30°N–30°S). A lower value of 300 m^2 s^{-1} was used for higher latitudes reflecting less solar heating than the tropics. Further details on the 1-D model are described in supporting information ST1.

2.1.4. The Diurnal Variation of Fire Plume Height

The meteorological effects on the diurnal variation, such as the variation of the atmospheric stability and boundary layer height (Sofiev et al., 2012; Val Martin et al., 2012) were simulated using hourly CFSR data. Another important factor is the diurnal variation of fire burning (e.g., Mu et al., 2011). We followed the

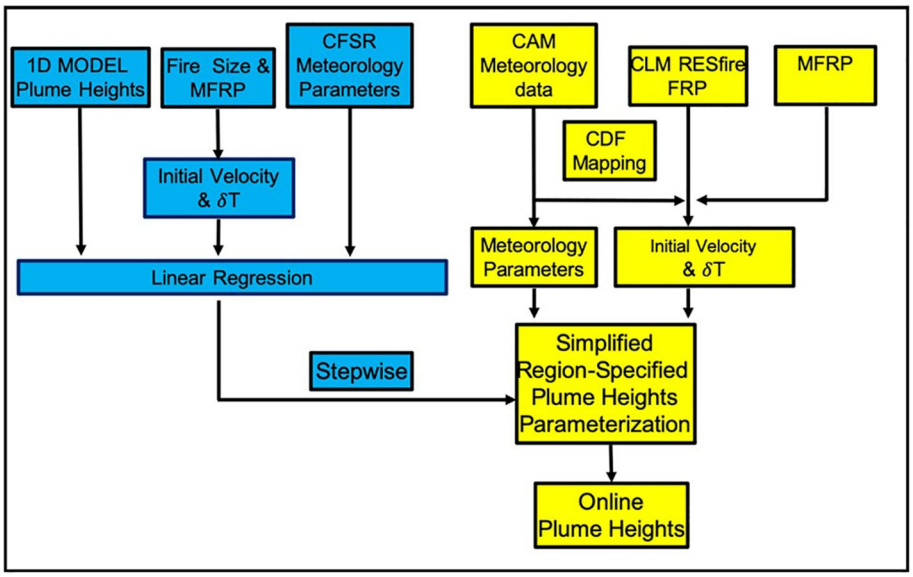

Figure 2. The schematic diagram of the CAM5 online fire plume height model implementation. The blue boxes represent the processes to develop the offline plume height parameterization. The yellow boxes the online parameterization. CAM5, Community Atmospheric Models version 5.

work by Ellicott et al. (2009) and Vermote et al. (2009) and parameterized the FRP diurnal variation using a modified Gaussian Function on the basis of the measurements by the Spinning Enhanced Visible and InfraRed Imager (SEVIRI)

$$FRP(t) = FRP_{peak} * \left[b + e^{\frac{-(t-h)^2}{2\sigma^2}} \right], \tag{4}$$

where the *FRP* is a function of time (hour), FRP_{peak} is the peak *FRP* value during a day at time h, b is a constant *FRP* value at night, and σ is the standard deviation value for the Gaussian function. The values of h, b, and δ were parameterized as functions of the observed Terra-to-Aqua FRP ratio (r)

$$h = -1.23r + 14.57 \tag{5}$$

$$\delta = 3.89r + 1.03 \tag{6}$$

$$b = 0.86r^2 - 0.52r + 0.08 \tag{7}$$

$$r = FRP_{terra} / FRP_{aqua}. \tag{8}$$

Since the parameterizations of Equations 4–8 for regional fires were based on hourly SEVIRI measurements, we computed the averaged regional r values using the MODIS MCD14ML products by selecting the measurements at local time 10:30 and 13:30 for Terra and Aqua satellites, respectively, from 2001 to 2014.

After calculating the r, b, δ, and h values for a given region, the FRP_{peak} value of a detected fire spot was determined by Equation 9

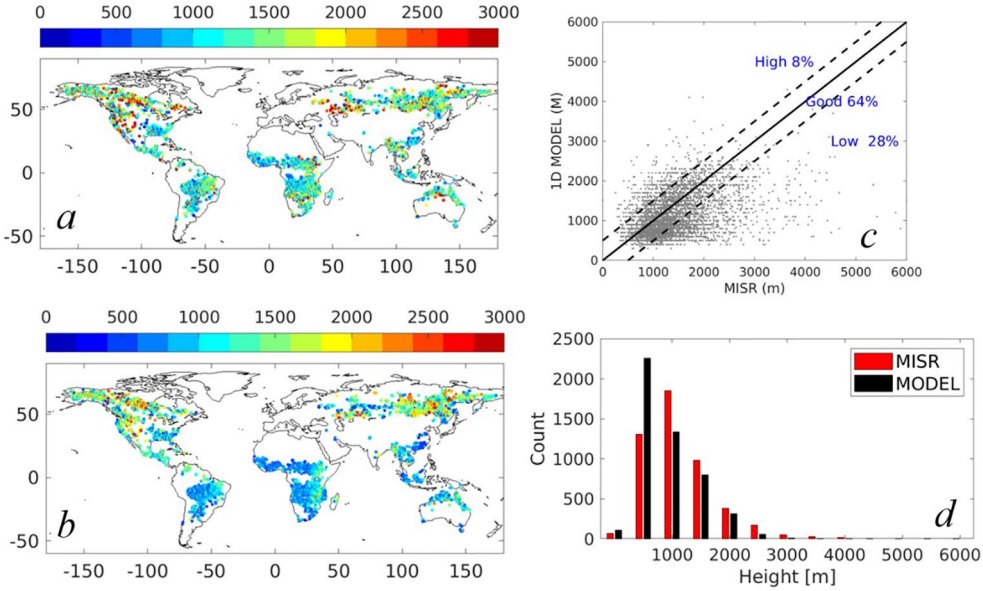

Figure 3. The comparison between MISR and 1-D model simulated (offline) fire plume heights. Panel a shows the MISR fire plume heights. Dots represent MISR (2002–2010) fire plumes and the color shading shows fire plume heights. Panel b is the same as panel a, but for 1-D model simulated results. Panel c shows MISR fire plume height and the corresponding 1-D model result for each MISR fire hotspot. Only 1-D model data corresponding to the MISR observation time and locations were used in the comparison. The central solid black line is the 1:1 line, with the two 500 m error lines are shown in dashed lines. Panel d is the histogram comparison between the MISR (red) and model simulated (black) fire plume height in an interval of 500 m. MISR, Multiangle Imaging SpectroRadiometer.

$$FRP_{peak} = FRP_T \Big/ \left(b + e^{\frac{-(t_T - h)^2}{2\sigma^2}} \right), \tag{9}$$

where FRP_T is the FRP value of a fire hotspot by Terra MODIS and t_T is the Terra overpass time during daytime, which is provided by MODIS MCD14ML products. Using Equation 4, we computed the hourly FRP values. The regional parameter values of b, δ, and h are listed in Table S4, and the regional diurnal FRP variation was calculated. For illustration purposes, we computed the typical regional MFRP diurnal profiles using Equation 9 (Figure S3).

Using Equations 1 and 2 and calculated FRP data, we computed hourly fire size $A(t)$ and total fire energy $E(t)$. These data and CSFR meteorology fields were applied to the 1-D fire plume-rise model (Section 2.1.3) to calculate plume heights (Figure 1).

2.1.5. MISR Fire Plume Heights

The plume height data sets from the original MISR plume height project and project 2 were used to evaluate offline 1-D fire plume model results (Gonzalez-Alonso et al., 2019; Sofiev et al., 2012; Val Martin et al., 2012, 2018; Veira et al., 2015b). This data set includes fire plumes from 2002 to 2010 over eight regions, Africa, Alaska, Canada, Indonesia, North America, Siberia, South America, and Southeast Asia (http://misr.jpl.nasa.gov/getData/accessData/MisrMinxPlumes/). The data availability is summarized in Tables S5 and S6. In this study, we only used the data with a "good" quality flag. The maximum MISR plume height of each hotspot was compared with the 1-D estimated fire plume height of the corresponding hotspot. A total of 14,800 MISR plumes were included in this study (Figure 3a). In general, the fire plume heights are higher in high latitudes and lower in low latitudes.

As both MISR and MODIS are onboard the Terra satellite, we found MODIS fire hotspots corresponding to MISR data. By obtaining the fire information, including location, time, FRP, from MCD14ML product, we

Table 1
Three Model Experiments to Investigate Fire Aerosol Effects

Experiment	Fire emission	Plume height
NO-Smk	Off	Off
Srf-Smk	On	Surface
Plm-Smk	On	Defined

calculated the fire plume heights using the 1-D model and compared the results to corresponding MISR data (Figure 3).

2.1.6. The AOD Data

The Cloud-Aerosol Lidar and Infrared Pathfinder Satellite Observations (CALIPSO) provide a multiyear global data set of lidar aerosol and cloud profiles with six identified aerosol types: clean marine, dust, polluted continental, clean continental, polluted dust, and smoke, measured by the Cloud-Aerosol Lidar with Orthogonal Polarization (CALIOP) instrument (Winker et al., 2010). Schuster et al. (2012) compared CALIPSO with AERONET AOD measurements at 147 AERONET sites and suggested a low bias of 13% in CALIPSO data due to a bias in the assumed lidar ratio. However, for biomass burning aerosols, the measurement bias is relatively low, and the measurement sensitivity of the CALIOP instrument is higher than MODIS (Ma, Bartlett, et al., 2013). In this study, we used the CALIPSO level 3 all-sky daytime monthly mean fire AOD data associated with a 2° × 5° resolution. Furthermore, the MODIS Collection six merged version of Dark-Target and Deep Blue monthly mean AOD product is also used in this study for model evaluation purposes (Sayer et al., 2013, 2014).

2.2. Model Experiments on the Sensitivity of Fire AOD Distribution to Plume Rise

In this study, we used the Community Earth System Model (CESM) version 1.2 in a configuration of the community atmosphere model version 5 (CAM5) (Neale et al., 2012) coupled with community land model version 4.5 (CLM4.5) (Oleson et al., 2013). The 3-mode Modal Aerosol Model (MAM3) is included in CAM5 to simulate the aerosol lifecycle (Liu et al., 2012). In MAM3, the aerosol mass and number mixing ratio were simulated in three lognormal modes: Aitken, accumulation, and coarse mode. BC and primary organic matter (POM) from wildfires and anthropogenic sources were emitted into the accumulation mode. The model horizontal resolution is 0.9 × 1.25 ° in latitude and longitude, respectively, with 30 vertical layers from the surface to the middle stratosphere (~40 km) (Neale et al., 2012).

Three model experiments were carried out to examine the effects of plume rise on fire AOD distribution: the control run without fire emissions (NO-Smk), the surface run with fire emissions released from the surface (Srf-Smk), and the fire plume run with fire emissions released at altitudes up to computed fire plume heights (Plm-Smk). The experiments are summarized in Table 1. The wildfire emissions used in the study were from GFED4s (Randerson et al., 2012), which has a 0.5° × 0.5° resolution and a 3-h temporal resolution. The emission data are available from 1997 to the present.

The model experiments were nudged to the NASA GEOS-5 reanalysis meteorology field U, V, and T. The fire emissions were the observation-based GFED inventory. As a result, we used offline 1-D model computed fire plume height data set in the Plm-Smk run. The fire emissions were distributed toward the top of a fire plume with a half-Gaussian shape as a function of height (Figure S4), which gives 0 emission at the surface and the maximum at the top (e.g., Freitas et al., 2010; Romp, 2010; Simpson & Wiggert, 1969; Yanai et al., 1973).

The model simulations were carried out for the period of 2004–2010. The first two years are used as spin-up and 2006–2010 data are used to analyze and compared to MODIS dark-target AOD and the CALIPSO fire AOD data, which became available since 2006. By comparing Plm-Smk to NO-smk results, we examined the effects of fires in the global AOD distribution, which was compared to CALIPSO data. By comparing Plm-Smk to Srf-Smk results, we analyzed the effects of plume-rise in AOD distribution, black, and organic carbon surface concentration.

2.3. Online Parameterization of Fire Plume Height in CESM

The offline observation-based fire plume height database described above cannot be used in a climate model directly since the climate model is not meant to reproduce the observed day-to-day weather, which strongly affects fire occurrences. Embedding the 1-D fire plume model in the climate model is computationally expensive and the results may have large systematic errors occasionally because of the biases of climate

simulations. We therefore developed an online parameterization to compute fire plume height for CESM. The online REgion-Specific ecosystem feedback Fire (RESFire) model that simulates fire occurrence and burned area in CAM5 and CLM4.5 was described by Zou et al. (2019). The fire, ecosystem, and meteorological parameters for computing fire plume height were computed by RESFire, CLM4.5, and CAM5, respectively. The online region-specific and PFT-specific parameterizations were based on the offline fire plume height data set and meteorological reanalysis data (Figure 2). It cannot be used in online climate model simulations directly because of systematic biases in simulated meteorological variables that are important for fire plume rise; we correct the model biases using a cumulative distribution function (CDF) mapping method in the same manner as Zou et al. (2019). An alternative is to use climate model meteorological data directly with the offline fire plume height data set. We chose not to do it for two reasons: (1) the weather data simulated by the climate model do not correspond to the observed fires in the offline data set; (2) any change of the climate model will require the construction of new online parameterizations.

2.3.1. Online Fire Plume Height Parameterization

The online region-specific fire plume-rise height parameterization is based on the statistical relationship between meteorological variables and the fire plume height data set (Figure 2) for the same 15 wildfire regions used to compute the data set (Figure S1). We used only MODIS detected hotspots with a confidence level of >95% from 2002 to 2010. The important parameters for fire plume height include the initial fire plume velocity and the temperature difference between fire and ambient air (Freitas et al., 2007, 2010; Latham, 1994; Turner, 1979). As in 1-D modeling, we calculated the initial velocity and temperature difference between fire and ambient air as functions of fire size, MFRP, surface air temperature, and surface pressure following Freitas et al. (2007). We found that fire plume initial velocity is better correlated with MISR observed fire plume height than FRP (Figure S5), which was used in previous studies (e.g., Doherty et al., 2013; Sofiev et al., 2012; Val Martin et al., 2012). Another important factor is boundary layer height (e.g., Sofiev et al., 2012), and this parameter is also included in our parameterization. In addition to the three parameters, initial fire plume velocity, the temperature difference between fire and ambient air, and the boundary layer height, we also considered other 24 terms derived from three meteorological parameters: the vertically potential temperature difference at an interval of 500 m from the surface to 6 km in altitude (12 terms), the horizontal wind speed at an interval of 500 m from the surface to 3 km (6 terms), and the specific humidity for the same layers as wind speed (6 terms). Including the constant term, a total of 28 terms were used in the linear regression process for a given fire region and PFT. By using the interactive stepwise multilinear regression function in MATLAB with a 0.01 threshold, the number of effective parameters was reduced from 28 to no >12. As plume heights have diurnal, seasonal, and regional variations, the parameterizations were developed to capture the hourly, monthly, and regional variations. The selected parameters and regression coefficients are listed in supporting information (selected_terms.txt and coefficients.txt), respectively. More details are in supporting information ST2.

2.3.2. CDF Mapping

Zou et al. (2019) discussed the large biases in estimated fires due to the systematic biases of the climate model simulations when the fire model was developed using the observations. The fire plume height parameterization developed here is based on MODIS fire hotspot observations and CSFR reanalysis meteorology data. We expected that direct application of this parameterization with CAM5 and CLM4.5 simulation results could lead to large biases in fire plume height estimates due in part to the biases in the fire parameters simulated by the climate model. As in Zou et al. (2019), we applied the CDF mapping method to correct the simulation biases (Piani et al., 2010; Teutschbein & Seibert, 2012). The CDFs of model simulated data were linearly mapped to those of the observation-reanalysis data such that the statistical distributions of mapped model data are the same as the observation-reanalysis data. In this manner, we reduced the mean biases of model data while maintaining the simulated dynamic variability. See Zou et al. (2019) for more details about the application of mapping to reduce biases.

Figure 2 illustrates the application of the CDF mapping in the online fire plume height parameterization. Since large diurnal variation of fire height was expected, hourly CDF mapping of meteorology data was applied. An example is shown for Boreal North America (BONA) in Figure S6. In addition to meteorological variables, we also needed to compute the initial velocity and temperature difference between fire and ambient air functions of fire size, MFRP, surface air temperature, and surface pressure (Freitas et al., 2007).

MFRP data were obtained from Terra MODIS observations with prescribed diurnal variations based on Terra and Aqua MODIS data described in Sections 2.1.3 and 2.1.4. Therefore, no CDF mapping is necessary. Hourly fire FRP data were estimated using the RESFire model (Zou et al., 2019) and we applied the CDF mapping of RESFire model FRP data to MODIS FRP data described in Section 2.1.1. Then we computed fire size by scaling CDF mapped FRP to MFRP of the grid cell (Section 2.1.2). The resulted fire size and MFRP were used to calculate the initial fire plume velocity and temperature difference, as described in Sections 2.1.2 and 2.1.3. Since FRP was based on model data, we applied the CDF mapping of fire size to the observation-based fire size data set described in Section 2.1.2. An example of the FRP CDF of BONA is shown in Figure S7. The resulting online plume height data were evaluated with the MISR observations with the results provided in the following section.

3. Results and Discussion

3.1. Evaluation of Observation-Constrained Fire Plume Height Simulations

The MISR fire plume heights are shown in Figure 3a. Due to the polar orbit, the MISR plume height data set has a higher sampling density over North America and Siberia, and a lower sampling density over the tropical region. The average fire plumes are >1,800 m over Alaska and Canada and >1,300 m over Siberia, while the fire plume heights are largely <1,200 m over South America and Africa. This pattern can be summarized as low in low latitudes and high in high latitudes. The offline 1-D model simulated fire plume heights (Figure 3b) largely agree with this latitudinal pattern, which is a major improvement compared to previous studies (Sofiev et al., 2012, 2013; Veira et al., 2015a). Since the tropical regions including South America, Africa, and Southeast Asia are most frequently burned regions over the world, the agreement with the MISR observations over these regions is important for accurately simulating the impacts of wildfire emissions on climate and pollution. Previous studies tend to greatly overestimate the fire plume heights in the tropics but underestimate in high latitudes. The overestimation in the tropics could lead to a high bias on the effects of black carbon on the Hadley circulation (Tosca et al., 2013, 2015). The underestimation of fire plume heights in high latitudes could affect transport of black carbon from the midlatitudes to the Arctic and the consequent snow and ice melting in the region (Keegan et al., 2014).

The points-to-point comparison between MISR and 1-D fire plume heights are shown in Figure 3c. The uncertainty level of the MISR data is 250–500 m (e.g., Nelson et al., 2013); we therefore consider model simulations within 500 m of MISR data "good" quality. About two-thirds of model data (64%) fall in this range, similar to the previous study (63%) by Sofiev et al. (2012). While the systematic low bias over high latitudes from the previous study was corrected (Veira et al., 2015b), our results still have a low bias when MISR fire plume heights are >3 km, probably due to the insufficient latent heat release in the 1-D plume-rise model. Another possibility is a low bias in the MODIS FRP data since dense smokes caused by intense fires would compromise the ability of MODIS sensor to detect the energy emitted by fires. The low bias for high-altitude fire plumes is also shown in the histogram comparison (Figure 3d). The simulated distribution shows that globally fire plume height occurrence frequency peaks at 750 m and decreases rapidly with increasing altitude, which is in good agreement with MISR observations. Overall, the 1-D model results captured the observed spatial and histogram distributions of fire plume height.

The diurnal variations of fire plume height are shown in Figure 4. As shown in Figure 3, the simulated average plume height is in good agreement with the MISR data. The simulated diurnal variation of plume rise, constrained by Terra and Aqua FRP observations, is similar to that of the PBL height. The average plume height value at 14:00, around the Aqua satellite overpass time, is 2,041 m, almost double the mean MISR-derived plume height of 1,300 m for 10:30 local time observations.

Figure 4 also shows the average fraction of fire plumes above the PBL observed by MISR at around 19%. We define a plume penetrating into the free troposphere when the maximum fire plume height is > the boundary layer height. Our calculated average MISR plume penetration fraction is smaller compared to the previous studies, 48% (Val Martin et al., 2010, 2012). Three factors may attribute to this difference. First, this study includes the global MISR height data of >14,000 plumes compared to 584 plumes over North America by Val Martin et al. (2012). The MISR plume heights over North America are much higher than over South America, Africa, and Southeast Asia (Figure 3), while the boundary layer height is higher over these tropical

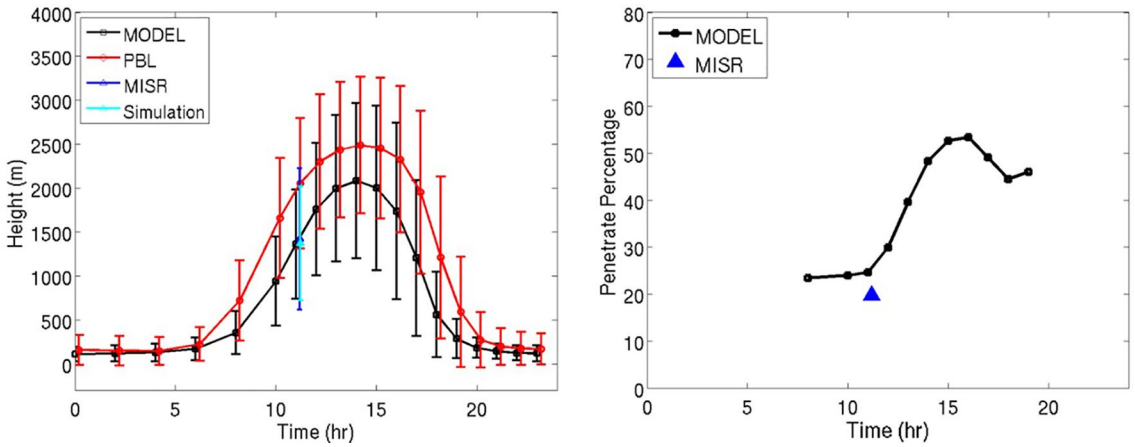

Figure 4. The simulated diurnal variation of the plume heights. The left panel shows the model simulated plume heights (black) and corresponding planetary boundary layer heights (red) vary as a function of time. The dots represent means, and the error bars represent the standard deviations. The MISR plume heights are shown in blue, and corresponding simulated heights are shown in cyan. The right panel shows the penetration rates of each hour for the daytime. The simulated penetration rates are shown in black, while the MISR observed penetration rate is in blue. MISR, Multiangle Imaging SpectroRadiometer.

regions compared to high latitudes at the time of MISR observations (Val Martin et al., 2018). Second, in the Val Martin et al. (2012) study, the boundary layer height data from GEOS has a temporary resolution of 3 h. Around the MISR observation time, it can vary a lot in the 3-h period (Figure 4). For example, it is around 800 m at 9:00 am and increases to 2,200 m at 12:00 pm. For the reason, we use the CSFR hourly data to minimize this uncertainty. Another reason is that different models define boundary layer height in different ways. The purpose of this study is not to give an absolute values of the penetration fraction, but to show that the penetration fraction increases rapidly from late morning to the late afternoon as the instability of the atmosphere increases.

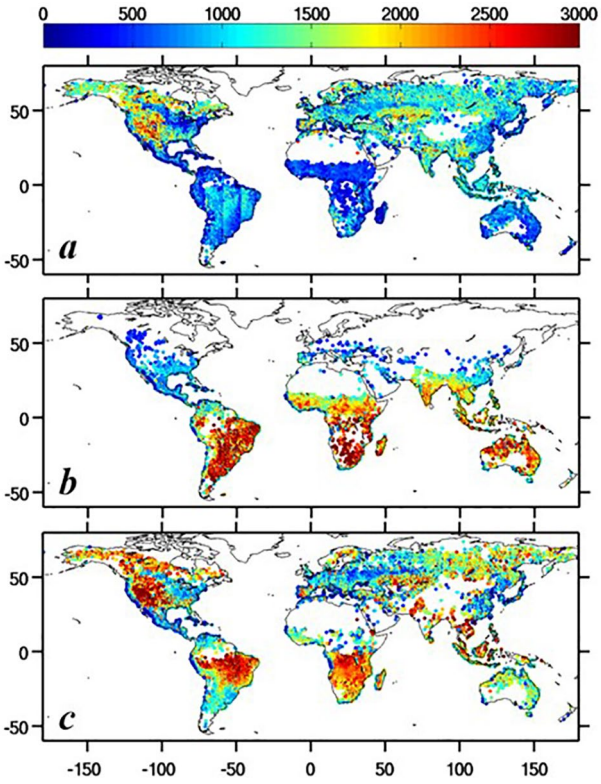

Figure 5. The mean of model simulated plume heights from 2002 to 2010. The panel a is the mean of plume heights at 11:00 am local time. The panel b is the mean of plume heights at 2:00 pm in January. The panel c is the same as panel b, but for July. The unit of height is meter.

The 1-D model simulated a somewhat higher above-PBL fraction of 25%. This fraction keeps on increasing till reaching a maximum of 53% at 15:00–16:00 in late afternoon. This also can be seen in the increasing overlap between the ranges of plume rise and PBL heights from 11:00 to 16:00 (Figure 4a). Accounting for the large increase of fire plume rise above the PBL in the afternoon, when most of the wildfire burning occurs based on satellite FRP observations (Ellicott et al., 2009; Vermote et al., 2009), implies that a higher fraction of wildfire plume reached the free troposphere than the fraction of ~20% estimated using MISR observations by Val Martin et al. (2012) and the resulting fire emissions of aerosols and gases underwent faster free-tropospheric transport than the boundary layer affecting larger geographical regions.

The observation-based 1-D model simulated plume-rise height distributions are shown in Figure 5. At the overpass time of Terra (11:00 am LT), the results fill the gaps in MISR observations (Figure 3) and show a general pattern of higher fire plume rise at high latitudes than the tropics. Fire plume heights at Alaska, Canada, western United States, and Siberia reach 1,500–3,000 m in comparison to 500–1,200 m in the tropical regions.

At 14:00 in January, fire plume heights are much higher in the Southern Hemisphere (SH), where most fires occur, than the Northern Hemisphere (NH). The SH fire plumes can reach 3,000 m in most regions whereas the NH plumes are largely <1,000 m due to a more unstable atmosphere and strong burning intensity in the SH. At 14:00 in July, wildfires over Alaska,

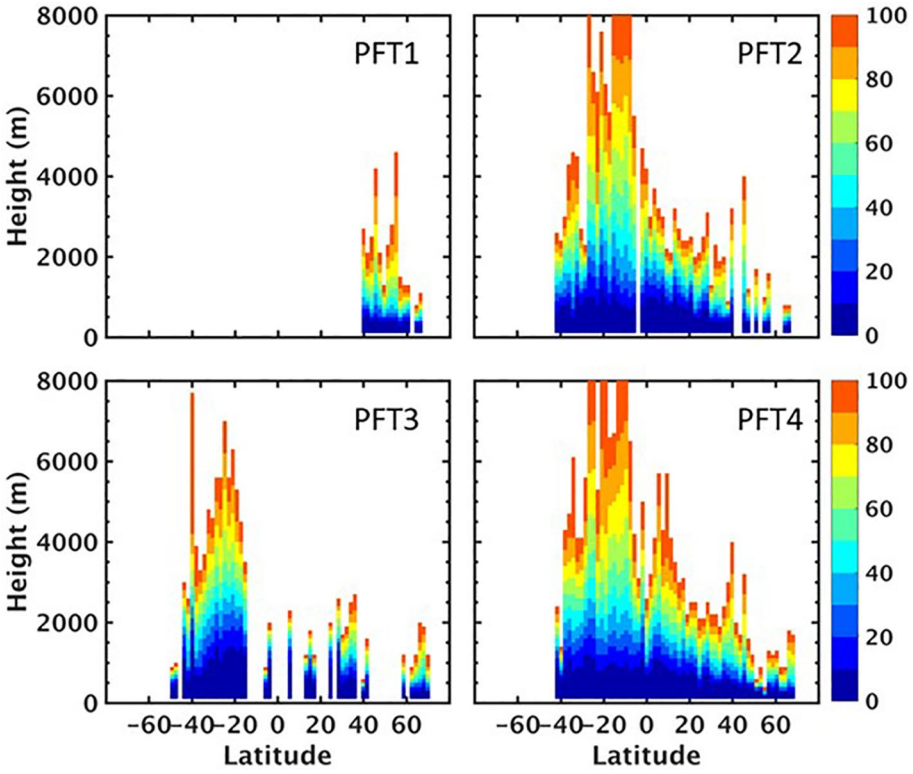

Figure 6. The zonal-mean emission distribution in January from 2002 to 2010. The shown distribution is the cumulative distribution from the surface to the top of the plume. The color shading shows the percentage for each 100-m interval. The PFT one to four represents the needle tree, broadleaf tree, shrub, and grass, respectively. More information about the PFT category and distribution is shown in Figure S2 and Table S2.

Canada, and western United States have highest fire plumes in the NH. The fire plume heights in Siberia are moderate because these fires tend to be tundra fires, which are less intense compared to other boreal forest fires (Wooster & Zhang, 2004). In the SH, tropical burning over the central South America and Africa has high fire plumes but not reaching the maxima of January burning in the regions. The observation-based distributions are in better agreement with limited MISR observations than Sofiev et al. (2012). More global observation data sets of fire plume heights, preferably in the afternoon from satellite instruments such as CALIOP and TROPOMI, are necessary to improve model simulations.

The zonal-mean cumulative vertical distribution of fire emission at 14:00 LT, when is the peak emission time in the GFED hourly emission data (Mu et al., 2011), is shown in Figures 6 and 7 for January and July, respectively. In January, as shown in Figure 5, most burning takes place in the tropical grass-savanna (PFT4) and forest (PFT2) (Giglio et al., 2013). Most fire emissions are released between 0°N and 20°N, where the median fire plume heights for PFT2 and PFT4 (dominant PFT, Figure S2) are at 1,500–2,000 m and the 75th percentile values reach 3,000 m (Figure 6). Our estimated fire emissions for the tropics are much higher in altitude than the 0–1,000 m distribution setting in the AeroCom protocol (Dentener et al., 2006), in which the tropical (30°S–30°N) fire emissions are distributed to 20% at 0–100 m, 40% at 100–500 m, and 40% at 500–1,000 m. Due in part to solar heating, fire plume heights in the southern tropics are higher than the northern tropics.

July is the month of most burning globally over eight fire regions: Boreal North America, Boreal Asia, West Temperate North America, Europe, Middle East, Central Asia, South Hemisphere South America, and South Hemisphere Africa (Giglio et al., 2013). Over the tropical SH (SHSA and SHAF) with frequent burning, the median fire plume heights of PFT2 and PFT4 are at 1,500–2,500 m and the 75th percentile heights reach the range of 2,500–3,000 m (Figure 7), much higher than the range of 0–1,000 m in AeroCom protocol (Dentener et al., 2006). In the NH temperate regions, the median fire plume heights of forests (PFT1 and

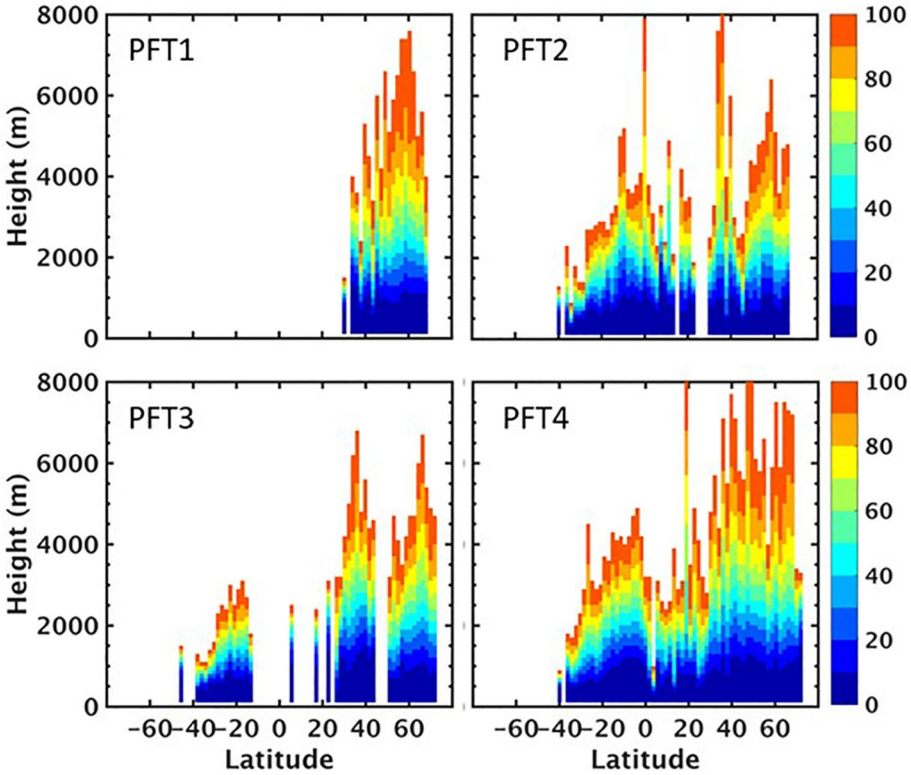

Figure 7. Same as the Figure 6 but for July.

PFT2) are at 2,000–2,500 m and the 75th percentile heights reach 3,500–4,000 m, while the median heights of grass-savanna (PFT4) burning are at 2,500–3,000 m and the 75th percentile height is up to 4,000 m. In comparison, the fire emission is released at 0–2,000 m in these regions in the AeroCom protocol (Dentener et al., 2006).

3.2. Effects of Plume Rise on AOD and Aerosol Concentrations

Zhang et al. (2020) evaluated model simulated AOD with MODIS observations, using the observation-constrained fire plume height data described here, over fire burning regions. There was a general agreement, but the GFED fire aerosol emissions have a low bias. The comparison between MODIS and model simulated AOD data are shown in Figure 8. The results shown here are similar to previous CAM5 simulations reported by Ghan et al. (2012) and Liu et al. (2012). In January, the strongest AOD signals are from north equatorial Africa, where both desert dust and wildfires contribute to AOD. The MODIS AOD has higher values in the downwind direction due most likely to the low bias in dust transport in the CAM5 model (Wu et al., 2020). Over the equatorial Africa, the MODIS AOD is higher than both Srf-Smk and Plm-Smk experiments. The relative AOD difference between the two experiments (without and with fire plume rise) is small (Figure 9) due to the dominant influence of dust AOD in this region in January. There are also low bias in the model over northern India and east China. However, there are little wildfire emissions in these regions in this month and the low bias are attributable to anthropogenic emissions.

Over the wildfire regions in July, like the northern hemisphere high latitudes, the southern hemisphere Africa and the south America, the MODIS AOD is also higher than model AOD (Figure 8). The CAM5 low biases in simulated AOD are prevalent over regions with fire, dust, and anthropogenic emissions. We focus in this study on the impact of plume rise in Figure 9b. The plume rise enhances AOD over the northern hemisphere high latitudes downwind from fire emissions by up to 20%, while there are slight AOD reductions over source regions. This overall AOD increment in the northern hemisphere high latitudes helps to reduce the low bias of the model simulated AOD compared to the observations (Jiang et al., 2016) if the

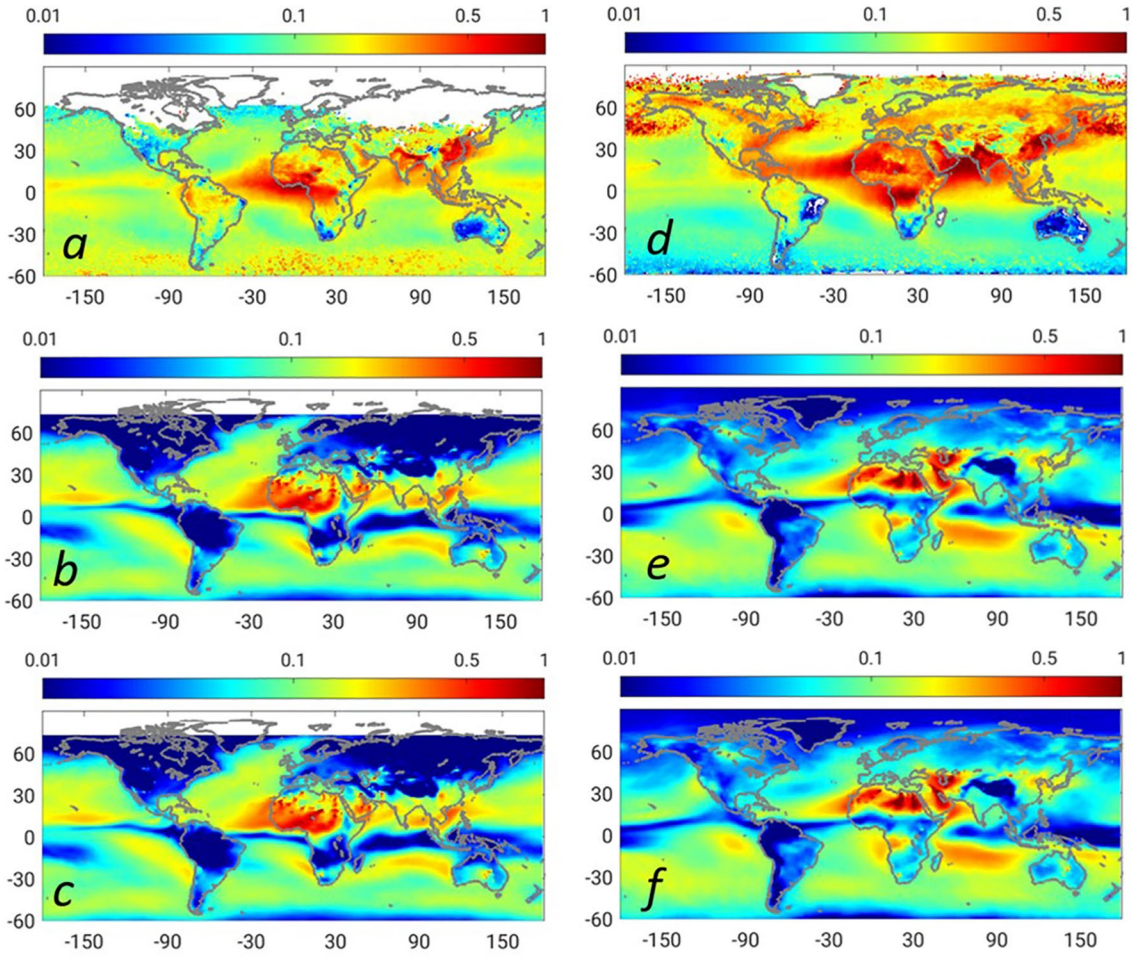

Figure 8. The comparison between MODIS measured and model simulated distributions of AOD data averaged between 2006 and 2010. The left column shows the mean AOD distributions in January from (a) MODIS, (b) Srf-Smk run, and (c) Plm-Smk run, respectively. The right column displays the mean AOD distributions in July from (d) MODIS, (e) Srf-Smk run, and (f) Plm-Smk run, respectively. The values shown in color shading are AOD values. AOD, aerosol optical depth.

wildfire emission can be significantly increased. Similar AOD enhancements are also found over the southern hemisphere Africa and the South America, where fire aerosols dominate.

In addition, we compare model simulated fire AOD with CALIPSO smoke AOD data (Omar et al., 2009), which are more specific for fire aerosols but also have relatively large uncertainties (Tackett et al., 2018). We

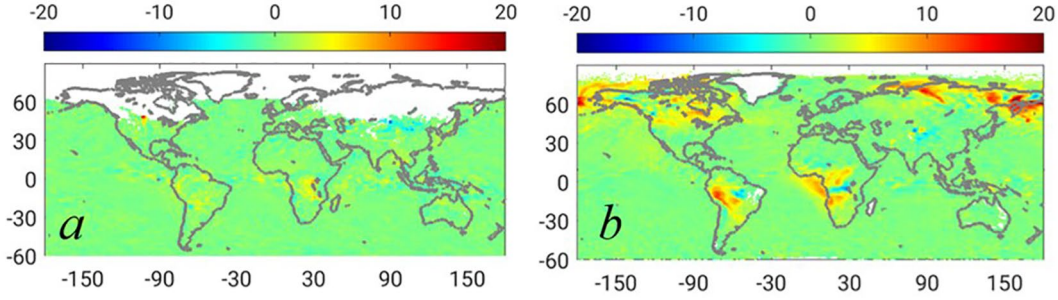

Figure 9. The relative difference between the Plm-Smk and Srf-Smk simulated AOD data in (a) January and in (b) July, averaged between 2006 and 2010. The values shown in color shading are the percentage changes of the Plm-Smk run relative to the Srf-Smk run. AOD, aerosol optical depth.

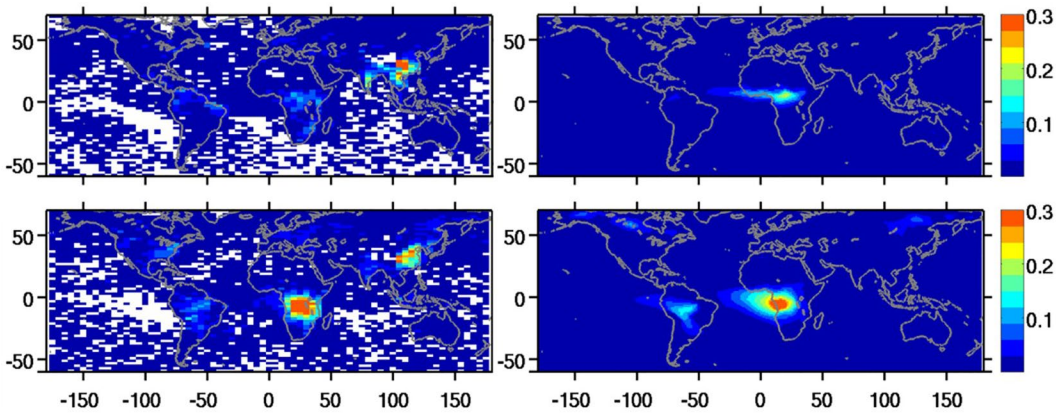

Figure 10. The comparison of the CALIPSO and the CAM5 simulated AOD. The upper left is the averaged CALIPSO smoke related AOD in January, while the bottom left is for July. The upper right is the averaged CAM5 simulated wildfire related AOD in January, while the bottom right is for July. CALIPSO, Cloud-Aerosol Lidar and Infrared Pathfinder Satellite Observations; CAM5, Community Atmospheric Models version 5; AOD, aerosol optical depth.

calculated the fire AOD distributions by subtracting the control run results (without fire emissions) from the simulation results with GFED4s fire emissions and the observation-based fire plume-rise data set. Observed and the corresponding model results for January and July during the period of 2006–2010 are shown in Figure 10. While observed and simulated data have similar spatial patterns, differences in details can be identified. The satellite smoke aerosol observation data tend to show high concentrations over industrialized regions, such as India and China in January, and China, western Europe, and eastern United States in July, where the model results show insignificant wildfire emissions. Over North America, the model shows high amounts of fire AOD over Alaska and Canada in July in contrast to higher smoke AOD data over eastern than western United States and Canada. It appears that satellite smoke retrievals over industrialized regions may have a high bias. Over the tropical burning region, model simulated fire AOD data tend to be higher than the satellite observations. In January, simulated African fire AOD data are higher than CALIPSO retrievals but lower in the northern South America. In July, simulated fire AOD data are higher over South America, but lower over Africa. Decreasing fire emissions may help improve the comparison with CALIPSO retrievals in the model. However, the model evaluations by Zhang et al. (2020) suggested that the model fire aerosol emissions have a low bias in general.

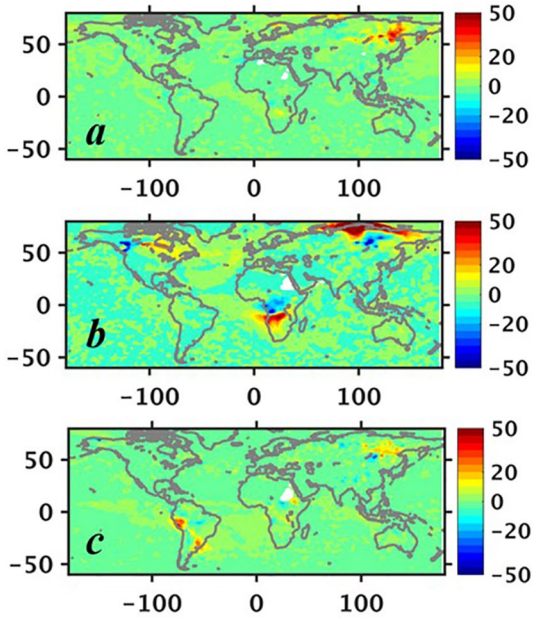

Figure 11. The impact of plumes on monthly AOD. The effect is represented by the percentage values of the AOD departures between plume smoke run and surface smoke run relative to the no-fire climatology AOD. The upper panel (a) is for May 2006, the middle panel (b) is for July 2006, and the bottom panel (c) is for September 2007. AOD, aerosol optical depth.

Some of the model and satellite retrieval differences may be related to uncertainties in fire plume-rise simulated in the model. We examine the effects of plume rise on fire AOD distribution by examining the AOD difference between the model simulation results with plume rise to those in which fire emissions were released in the surface layer. Figure 4 shows that fire plume rise above the top of the boundary layer usually occur in daytime. Therefore, the differences of AOD distribution between the two model simulations are due to daytime mixing, when fire aerosols released in the surface layer can be easily mixed into the boundary layer. This suggests short-term AOD variability in addition to the long-term difference shown above. A recent study (Zhu et al., 2018) also suggested that the model simulations with a fire plume parameterization would show larger differences for specified plume events. Therefore, we selected three typical summer months in Figure 11 to show that the largest changes of fire AOD occurred in the region with large wind shear between the boundary layer and free troposphere. Fire AOD tends to increase in the downwind regions of free-tropospheric transport and decrease in the downwind

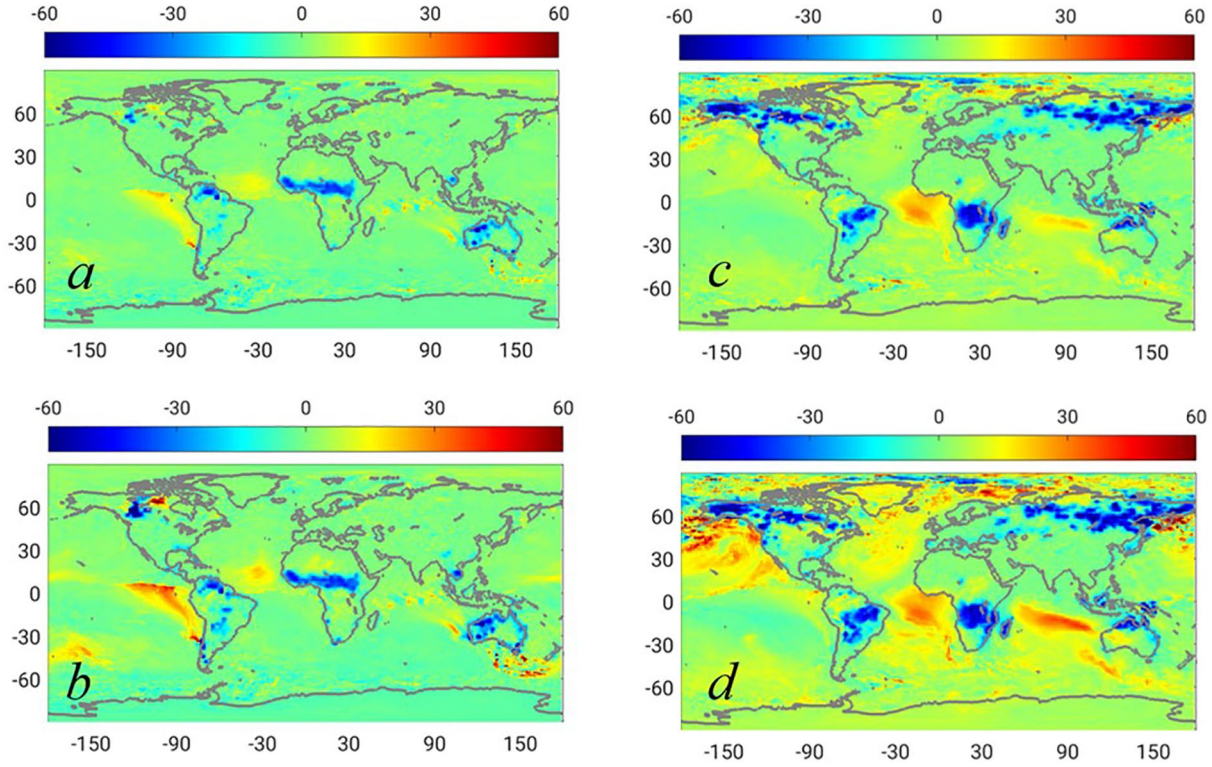

Figure 12. The relative differences between the Plm-Smk and Srf-Smk runs for simulated surface-layer BC and POM concentrations. The values shown in color shading are percentage changes of the Plm-Smk run relative to the Srf-Smk run. The percentage differences in surface black carbon concentrations in January and July are shown in panels (a) and (c), respectively. Panels (b) and (d) show the percentage differences in surface POM concentration in January and July. POM, primary organic matter.

regions of boundary-layer transport. Although the relative changes can be as large as 20–50% in some regions where background AOD is low and fire impact is large. However, the fire-induced absolute AOD changes are small relative to the differences between observed and simulated AOD data (Zhang et al., 2020).

The impacts of the plume rise on simulated surface-layer BC and POM are shown in Figure 12. In January, plume rise reduces surface BC concentrations over the north hemisphere Africa fire region by >30% but increases surface BC concentrations over the downwind Atlantic Ocean by up to 10%. The lower surface concentrations in the source region but higher surface concentrations in the downwind regions reflects stronger fire aerosol transport from the source region in the free troposphere with fire plume rise. The same effect is also shown over Australia and South America fire regions in the south hemisphere, as well as over Canada in the north hemisphere. The effects on surface POM concentrations are similar to BC; the magnitude is mostly larger because the emission ratio of POM to BC is higher in wildfire than anthropogenic emissions. The relative effects of fire plume rise are larger in July than January at northern midlatitudes and southern tropical and subtropical regions because the fire emissions are higher in those regions in July than January.

While plume rise clearly changes surface fire aerosol concentrations (Figure 12) and AOD (Figure 9) in model simulations for given fire emissions, the observations of AOD from satellite instruments such as MODIS do not provide good constraints on fire plume rise. AOD is a column integrated quantity, which includes aerosols from nonfire sources and is not very sensitive to vertical distribution. Therefore, the plume-rise effect at a selected layer, such as the surface, is larger than the column integrated AOD. A further problem is the large underestimate of CAM5 simulated AOD compared to MODIS observations (e.g., Jiang et al., 2016; Liu et al., 2012; Zhang et al., 2020) due to multiple reasons such as dust emission and transport (Wu et al., 2020), atmospheric circulations (Ma, Rasch, et al., 2013), aerosol treatments (Liu et al., 2012, 2016), and fire emissions (Zhang et al., 2020).

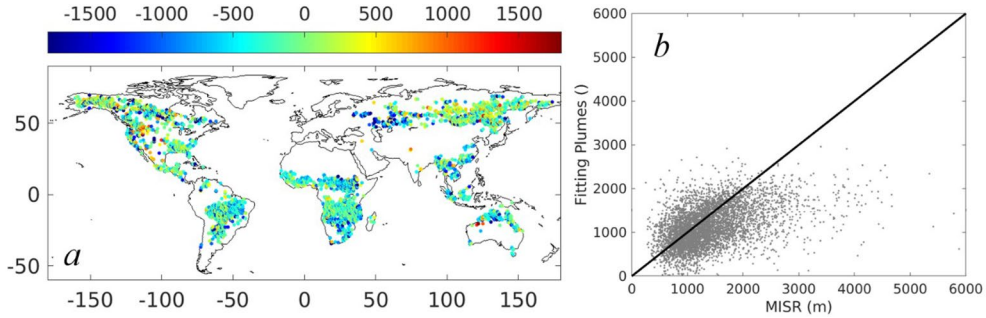

Figure 13. The verification for linear parameterization. The left panel (a) is the comparison between the simulated plume heights resulted from Stepwise simplified parameterization and the MISR plume heights. The color shading represents the value of the departure range from −1,800 to 1,800 m. The right panel (b) is a comparison between MISR heights and simulated results. MISR, Multiangle Imaging SpectroRadiometer.

For direct radiative forcing, AOD is important. However, the effect of fire aerosols through aerosol-cloud forcing is much larger than direct radiative forcing (e.g., Zou et al., 2019). The vertical distribution of fire aerosols matters more significantly for aerosol-cloud than direct radiative forcing because the former is more altitude dependent. Therefore, climate models may be more sensitive to fire plume-rise simulations than found in previous chemical-tracer studies by Veira et al. (2015a, 2015b) and Zhu et al. (2018). For air quality applications, surface concentrations are most important for human health. Figure 12 shows that plume rise can significantly decrease surface concentrations in source regions but increase surface concentrations downwind from fire regions. Considering the large diurnal variation (Figure 4) and the potential impact of climate change on plume rise and boundary layer height, the inclusion of computationally efficient fire plume-rise algorithm is important for assessing the effects of fire plume rise and its climate response and for reducing one of the uncertainties in climate assessments of fires.

3.3. Online Fire Plume-Rise Implementation

The comparison between MISR observations and the online parameterization results are shown in Figure 13. The input data used for online parameterizations are the same as the 1-D fire plume-rise data set. The general distribution features are similar. For example, tropical fire plume-rise heights are lower than at northern midlatitude and high latitude, in agreement with MISR observations (Figure 3), improving upon the previous studies (e.g., Sofiev et al., 2012, 2013). However, the low biases over Canada, western United States, and Siberia, where fire plumes are often higher than 2–3 km, are worse than the 1-D fire plume-rise data set (Figure 3), similar to the results by Sofiev et al. (2012, 2013). The larger biases of the online parameterizations, in which linear regression of fire plume-rise height with fire and meteorological parameters are considered, than the 1-D dynamic model results reflect the importance of nonlinear meteorological processes (e.g., Equation 3). Incorporating nonlinear dynamic processes will likely be a useful pathway to improve the online parameterizations of fire plume rise.

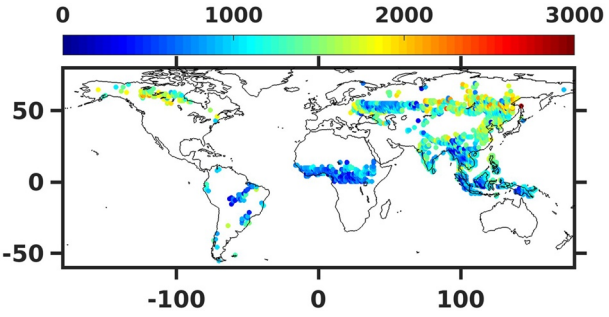

Figure 14. The plume heights produced by the CAM5 plume-rise implementation. The color shading represents plume heights (meters). The plume heights in the meter are for local time 11:00 in the morning. CAM5, Community Atmospheric Models version 5.

The online parameterizations must deal with various biases of the climate model simulations. We made use of the CDF mapping method (Section 2; Zou et al., 2019). To evaluate the performance of the online plume-rise parameterizations, we ran the CESM with coupled CAM-CLM components for one full year. As a fully coupled simulation, it is not possible to reproduce the meteorology conditions exactly like the conditions of MISR measurements. Therefore, we used the monthly mean plume-rise heights in the evaluation. The results are shown in Figure 14 Since fire burned areas are simulated using the RESFire model by Zou et al. (2019), the locations of simulated fires do not necessary overlap with the time periods of MISR-derived fire plume-rise height data. As a result, the pattern of fire distribution in Figure 14 differs from Figure 13.

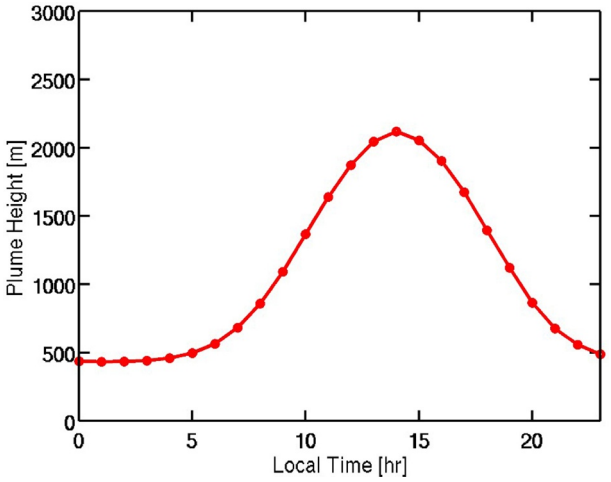

Figure 15. The diurnal cycle of the averaged plume heights in July from CESM. CESM, Community Earth System Model.

The general pattern of coupled plumes is similar as MISR data (Figure 3): higher fire plumes in midlatitude and high latitude and lower fire plumes in the tropics. The quality of fire plume-rise simulation is similar as using offline data (Figure 3). The averaged diurnal cycle of fire plume-rise height in July is shown in Figure 15. The diurnal cycle resembles that of the observation-constrained 1-D model computed data set (Figure 4), peaking at 14:00 local time with a maximum height at around 2 km. The nocturnal plume height is overestimated in CAM5 compared to the data used in 1-D fire plume modeling (Figure 4). We suggest that CDF mapping is applied separately for nocturnal model input parameters to reduce this bias in future studies.

4. Conclusions

We developed an observation-based global fire plume-rise data set for 2002–2010, using a modified 1-D plume-rise model on the basis of observed fire size and MFRP data as a function of plant functional type (PFT) for different regions. This study developed long-term plume height data set through using modified 1-D plume-rise model and region-specific and PFT-specific MFRP and fire size data as inputs, as well as CFSR meteorology variables. Compared to corresponding MISR data in the morning, the observed general geographical distribution feature is well captured: lower in the tropics and higher at northern midlatitude and high latitude, improving over the previous results of higher fire plume-rise heights in the tropics than midlatitude and high latitude (Sofiev et al., 2012; Veira et al., 2015b).

The diurnal variations of fire plume rise due to the changes of fire size and FRP and boundary-layer mixing were assessed. The key parameter for the impacts of fire emissions is the fraction of fire plumes penetrating above the boundary layer, which tends to increase during the day as the boundary layer is destabilized and fires intensify. While at the time of MISR observation (10:30 am LT) it is relatively low at 20%, the fraction increases to an average of ~55% in the late afternoon. The resulting fire emission vertical distributions show much more fire emissions at higher altitudes in the tropical and temperate regions than the zonal-mean emission distributions specified by the AeroCom Protocol (Dentener et al., 2006), which is widely used in the climate model simulations. Comparing model simulations using observation-based global fire plume-rise data set to those assuming surface emissions only, we found 20–50% fire caused monthly BC and POM concentration variation globally, suggesting larger effects of fire emitted aerosols in downwind regions on air quality and radiative and cloud forcing.

Using the 2002–2010 observation-based data set, we developed online fire plume-rise height parameterizations for 15 global wildfire regions using up to 28 terms for use in climate model simulations. While the general geographical distribution of the computed fire plume-rise height is reasonable, the parameterization has a considerably larger low bias than the 1-D model computed data when compared to MISR observations. The low biases are similar in magnitude to the previous results by Sofiev et al. (2012, 2013). The low biases are likely due to the use of linear regression in our study; the nonlinear dynamics of fire plumes could be represented better using the 1-D modeling approach (Frietas et al., 2007, 2010). We recommend investigating computationally efficient nonlinear regression-based parameterizations in future studies to improve the representation of fire plume rise in climate models. Furthermore, MISR-like global observations of fire plume heights, particularly in the afternoon, are necessary to improve our understanding of fire plume-rise processes, model simulations, and climate model parameterizations.

Data Availability Statement

Data used in this study are available from the following locations: CFSR meteorology hourly data: https://rda.ucar.edu/datasets/ds094.2/; MODIS MCD14DL (fire hotspot) data: https://earthdata.nasa.gov/earth-observation-data/near-real-time/firms; MISR plume heights data: https://misr.jpl.nasa.gov/getData/accessData/

MISRPlumeHeight/; CESM-CAM5: http://www.cesm.ucar.edu/models/; CALIPSO data: http://www.cesm.ucar.edu/models/. The data and source code produced by this study: https://doi.org/10.18738/T8/68P70B.

Acknowledgments
This work was supported by the National Science Foundation (NSF) through Grant 1243220. We thank Ralph Kahn and two anonymous reviewers for their comments and suggestions that improved this work. We would like to acknowledge high-performance computing support from Yellowstone (ark:/85065/d7w3xhc) and Cheyenne (https://doi.org/10.5065/D6RX99HX) supper computers provided by NCAR's CISL, sponsored by the National Science Foundation.

References

Allen, R. J., Sherwood, S. C., Norris, J. R., & Zender, C. S. (2012). Recent Northern Hemisphere tropical expansion primarily driven by black carbon and tropospheric ozone. *Nature*, *485*(7398), 350–354. https://doi.org/10.1038/nature11097

Bauer, S. E., & Menon, S. (2012). Aerosol direct, indirect, semidirect, and surface albedo effects from sector contributions based on the IPCC AR5 emissions for preindustrial and present-day conditions. *Journal of Geophysical Research*, *117*, D01206. https://doi.org/10.1029/2011JD016816

Boucher, O., Randall, D., Artaxo, P., Bretherton, C., Feingold, G., Forster, P., et al. (2013). *IPCC AR5 clouds and aerosols. Climate change 2013: The physical science basis. Contribution of working group I to the fifth assessment report of the intergovernmental panel on climate change*. https://doi.org/10.1017/CBO9781107415324.016

Browman, D. M. J. S., Balch, J. K., Artaxo, P., Bond, W. J., Carlson, J. M., Cochrane, M. A., et al. (2009). Fire in the Earth System. *Science*, *324*(5926), 481–484. https://doi.org/10.1126/science.1163886

Channan, S., Collins, K., & Emanuel, W. R. (2014). *Global mosaics of the standard MODIS land cover type data (30)*. College Park, MD: University of Maryland and the Pacific Northwest National Laboratory.

de Gouw, J. A., Warneke, C., Stohl, A., Wollny, A. G., Brock, C. A., Cooper, O. R., et al. (2006). Volatile organic compounds composition of merged and aged forest fire plumes from Alaska and western Canada. *Journal of Geophysical Research*, *111*, D10303. https://doi.org/10.1029/2005JD006175

Dentener, F., Kinne, S., Bond, T., Boucher, O., Cofala, J., Generoso, S., et al. (2006). Emissions of primary aerosol and precursor gases in the years 2000 and 1750, prescribed data-sets for AeroCom. *Atmospheric Chemistry and Physics Discussions*, *6*(2), 2703–2763. https://doi.org/10.5194/acp-6-4321-2006

Dirksen, R. J., Folkert Boersma, K., De Laat, J., Stammes, P., Van Der Werf, G. R., Martin, M. V., & Kelder, H. M. (2009). An aerosol boomerang: Rapid around-the-world transport of smoke from the December 2006 Australian forest fires observed from space. *Journal of Geophysical Research*, *114*, D21201. https://doi.org/10.1029/2009JD012360

Ditas, J., Ma, N., Zhang, Y., Assmann, D., Neumaier, M., Riede, H., et al. (2018). Strong impact of wildfires on the abundance and aging of black carbon in the lowermost stratosphere. *Proceedings of the National Academy of Sciences of the United States of America*, *115*(50)–E11603. https://doi.org/10.1073/pnas.1806868115

Doherty, S. J., Dang, C., Hegg, D. A., Zhang, R. R., Warren, S. G., Ames, R. B., et al. (2013). Modeling of biomass smoke injection into the lower stratosphere by a large forest fire (Part II): Sensitivity studies. *Atmospheric Chemistry and Physics*, *6*(4), 5261–5277. https://doi.org/10.5194/acpd-6-6081-2006

Ellicott, E., Vermote, E., Giglio, L., & Roberts, G. (2009). Estimating biomass consumed from fire using MODIS FRE. *Geophysical Research Letters*, *36*, L13401. https://doi.org/10.1029/2009GL038581

Evangeliou, N., Balkanski, Y., Hao, W. M., Petkov, A., Silverstein, R. P., Corley, R., et al. (2016). Wildfires in Northern Eurasia affect the budget of black carbon in the Arctic. A 12-year retrospective synopsis (2002–2013). *Atmospheric Chemistry and Physics Discussions*, *16*(12), 7587–7604. https://doi.org/10.5194/acp-2015-994

Freeborn, P. H., Wooster, M. J., Hao, W. M., Ryan, C. A., Nordgren, B. L., Baker, S. P., & Ichoku, C. (2008). Relationships between energy release, fuel mass loss, and trace gas an aerosol emissions during laboratory biomass fires. *Journal of Geophysical Research*, *113*, D01301. https://doi.org/10.1029/2007JD008679

Freitas, S. R., Longo, K. M., Chatfield, R., Latham, D., Silva Dias, M. A. F., Andreae, M. O., et al. (2007). Including the sub-grid scale plume rise of vegetation fires in low resolution atmospheric transport models. *Atmospheric Chemistry and Physics*, *7*(13), 3385–3398. https://doi.org/10.5194/acp-7-3385-2007

Freitas, S. R., Longo, K. M., Trentmann, J., & Latham, D. (2010). Technical note: Sensitivity of 1-D smoke plume rise models to the inclusion of environmental wind drag. *Atmospheric Chemistry and Physics*, *10*(2), 585–594. https://doi.org/10.5194/acp-10-585-2010

Ghan, S. J., Liu, X., Easter, R. C., Zaveri, R., Rasch, P. J., Yoon, J.-H., & Eaton, B. (2012). Toward a minimal representation of aerosols in climate models: Comparative decomposition of aerosol direct, semidirect, and indirect radiative forcing. *Journal of Climate*, *25*(19), 6461–6476. https://doi.org/10.1175/jcli-d-11-00650.1

Giglio, L. (2013). *MODIS collection 5 active fire product user's guide version 2.4*. College Park, MD: University of Maryland. Retrieved from http://198.118.255.205/sites/default/files/field/document/MODIS_Fire_users_Guide_2.4.pd

Giglio, L., Randerson, J. T., & Van Der Werf, G. R. (2013). Analysis of daily, monthly, and annual burned area using the fourth-generation global fire emissions database (GFED4). *Journal of Geophysical Research: Biogeosciences*, *118*, 317–328. https://doi.org/10.1002/jgrg.20042

Gonzalez-Alonso, L., Val Martin, M., & Kahn, R. A. (2019). Biomass-burning smoke heights over the Amazon observed from space. *Atmospheric Chemistry and Physics*, *19*, 1685–1702. https://doi.org/10.5194/acp-19-1685-2019

Grell, G., Freitas, S. R., Stuefer, M., & Fast, J. (2011). Inclusion of biomass burning in WRF-Chem: Impact of wildfires on weather forecasts. *Atmospheric Chemistry and Physics*, *11*(11), 5289–5303. https://doi.org/10.5194/acp-11-5289-2011

Hodnebrog, Ø., Myhre, G., Forster, P. M., Sillmann, J., & Samset, B. H. (2016). Local biomass burning is a dominant cause of the observed precipitation reduction in southern Africa. *Nature Communications*, *7*, 11236. https://doi.org/10.1038/ncomms11236

Jiang, Y., Lu, Z., Liu, X., Qian, Y., Zhang, K., Wang, Y., & Yang, X.-Q. (2016). Impacts of global open-fire aerosols on direct radiative, cloud and surface-albedo effects simulated with CAM5. *Atmospheric Chemistry and Physics*, *16*(23), 14805–14824. https://doi.org/10.5194/acp-16-14805-2016

Kahn, R. A., Chen, Y., Nelson, D. L., Leung, F. Y., Li, Q., Diner, D. J., & Logan, J. A. (2008). Wildfire smoke injection heights: Two perspectives from space. *Geophysical Research Letters*, *35*, L04809. https://doi.org/10.1029/2007GL032165

Kahn, R. A., Li, W. H., Moroney, C., Diner, D. J., Martonchik, J. V., & Fishbein, E. (2007). Aerosol source plume physical characteristics from space-based multiangle imaging. *Journal of Geophysical Research*, *112*, D11205. https://doi.org/10.1029/2006JD007647

Keegan, K. M., Albert, M. R., McConnell, J. R., & Baker, I. (2014). Climate change and forest fires synergistically drive widespread melt events of the Greenland Ice Sheet. *Proceedings of the National Academy of Sciences of the United States of America*, *111*(22), 7964–7967. https://doi.org/10.1073/pnas.1405397111

Latham, D. (1994). LUMP: A one-dimensional plume predictor and cloud model for fire and smoke managers. General Technical Report INT-GTR-314, Intermountain Research Station (11526, pp. 11528–11529). USDA Forest Service.P

Liu, X., Easter, R. C., Ghan, S. J., Zaveri, R., Rasch, P., Shi, X., et al. (2012). Toward a minimal representation of aerosols in climate models: Description and evaluation in the Community Atmosphere Model CAM5. *Geoscientific Model Development*, *5*(3), 709–739. https://doi.org/10.5194/gmd-5-709-2012

Liu, X., Ma, P.-L., Wang, H., Tilmes, S., Singh, B., Easter, R. C., et al. (2016). Description and evaluation of a new four-mode version of the Modal Aerosol Module (MAM4) within version 5.3 of the Community Atmosphere Model. *Geoscientific Model Development*, *9*(2), 505–522. https://doi.org/10.5194/gmd-9-505-2016

Liu, Y. (2004). Variability of wildland fire emissions across the contiguous United States. *Atmospheric Environment*, *38*(21), 3489–3499. https://doi.org/10.1016/j.atmosenv.2004.02.004

Liu, Y., Goodrick, S., & Heilman, W. (2014). Wildland fire emissions, carbon, and climate: Wildfire-climate interactions. *Forest Ecology and Management*, *317*, 80–96. https://doi.org/10.1016/j.foreco.2013.02.020

Ma, P.-L., Rasch, P. J., Wang, H., Zhang, K., Easter, R. C., Tilmes, S., et al. (2013). The role of circulation features on black carbon transport into the Arctic in the Community Atmosphere Model version 5 (CAM5). *Journal of Geophysical Research: Atmospheres*, *118*, 4657–4669. https://doi.org/10.1002/jgrd.50411

Ma, X., Bartlett, K., Harmon, K., & Yu, F. (2013). Comparison of AOD between CALIPSO and MODIS: Significant differences over major dust and biomass burning regions. *Atmospheric Measurement Techniques*, *6*(9), 2391–2401. https://doi.org/10.5194/amt-6-2391-2013

Madden, J. M., Mölders, N., & Sassen, K. (2015). Assessment of WRF/Chem simulated vertical distributions of particulate matter from the 2009 minto flats south wildfire in interior Alaska by CALIPSO total backscatter and depolarization measurements. *Open Journal of Air Pollution*, *4*, 119–138. https://doi.org/10.4236/ojap.2015.43012

Monks, S. A., Arnold, S. R., & Chipperfield, M. P. (2012). Evidence for El Niño-Southern Oscillation (ENSO) influence on Arctic CO interannual variability through biomass burning emissions. *Geophysical Research Letters*, *39*, L14804. https://doi.org/10.1029/2012GL052512

Mu, M., Randerson, J. T., Van Der Werf, G. R., Giglio, L., Kasibhatla, P., Morton, D., et al. (2011). Daily and 3-hourly variability in global fire emissions and consequences for atmospheric model predictions of carbon monoxide. *Journal of Geophysical Research*, *116*, D24303. https://doi.org/10.1029/2011JD016245

Myrup, L. O., & Ranzieri, A. J. (1976). A consistent scheme for estimating diffusivities to be used in air quality models. *Caltrans*

Neale, R. B., Chen, C.-C., Gettelman, A., Lauritzen, P. H., Park, S., Williamson, D. L., et al. (2012). Description of the NCAR community atmosphere model (CAM 5.0). *NCAR Tech. Note NCAR/TN-486+ STR*. https://doi.org/10.3390/rs5094593

Nelson, D., Garay, M., Kahn, R., & Dunst, B. (2013). Stereoscopic height and wind retrievals for aerosol plumes with the MISR INteractive eXplorer (MINX). *Remote Sensing*, *5*(9), 4593–4628. https://doi.org/10.3390/rs5094593

Oleson, K. W., Lawrence, D. M., Bonan, G. B, Drewniak, B., Huang, M., Koven, C., et al. (2013). *Technical description of version 4.5 of the Community Land Model (CLM).* (NCAR Technical Note). https://doi.org/10.5065/D6RR1W7M

Omar, A. H., Winker, D. M., Vaughan, M. A., Hu, Y., Trepte, C. R., Ferrare, R. A., et al. (2009). The CALIPSO automated aerosol classification and lidar ratio selection algorithm. *Journal of Atmospheric and Oceanic Technology*, *26*(10), 1994–2014. https://doi.org/10.1175/2009jtecha1231.1

Paugam, R., Wooster, M., Freitas, S., & Val Martin, M. (2016). A review of approaches to estimate wildfire plume injection height within large-scale atmospheric chemical transport models. *Atmospheric Chemistry and Physics*, *16*(2), 907–925. https://doi.org/10.5194/acp-16-907-2016

Pfister, G. G., Avise, J., Wiedinmyer, C., Edwards, D. P., Emmons, L. K., Diskin, G. D., et al. (2011). CO source contribution analysis for California during ARCTAS-CARB. *Atmospheric Chemistry and Physics*, *11*(15), 7515–7532. https://doi.org/10.5194/acp-11-7515-2011

Piani, C., Weedon, G. P., Best, M., Gomes, S. M., Viterbo, P., Hagemann, S., & Haerter, J. O. (2010). Statistical bias correction of global simulated daily precipitation and temperature for the application of hydrological models. *Journal of Hydrology*, *395*(3–4), 199–215. https://doi.org/10.1016/j.jhydrol.2010.10.024

Randerson, J. T., Chen, Y., Van Der Werf, G. R., Rogers, B. M., & Morton, D. C. (2012). Global burned area and biomass burning emissions from small fires. *Journal of Geophysical Research*, *117*, G04012. https://doi.org/10.1029/2012JG002128

Saha, S., Moorthi, S., Wu, X., Wang, J., Nadiga, S., Tripp, P., et al. (2014). The NCEP climate forecast system version 2. *Journal of Climate*, *27*(6), 2185–2208. https://doi.org/10.1175/jcli-d-12-00823.1

Sayer, A. M., Hsu, N. C., Bettenhausen, C., & Jeong, M.-J. (2013). Validation and uncertainty estimates for MODIS Collection 6 "deep Blue" aerosol data. *Journal of Geophysical Research: Atmospheres*, *118*, 7864–7872. https://doi.org/10.1002/jgrd.50600

Sayer, A. M., Munchak, L. A., Hsu, N. C., Levy, R. C., Bettenhausen, C., & Jeong, M. J. (2014). Modis collection 6 aerosol products: Comparison between aqua's e-deep blue, dark target, and "merged" data sets, and usage recommendations. *Journal of Geophysical Research: Atmospheres*, *119*, 13965–13989. https://doi.org/10.1002/2014JD022453

Schuster, G. L., Vaughan, M., MacDonnell, D., Su, W., Winker, D., Dubovik, O., et al. (2012). Comparison of CALIPSO aerosol optical depth retrievals to AERONET measurements, and a climatology for the lidar ratio of dust. *Atmospheric Chemistry and Physics*, *12*(16), 7431–7452. https://doi.org/10.5194/acp-12-7431-2012

Simpson, J., & Wiggert, V. (1969). Models of precipitating cumulus towers. *Monthly Weather Review*, *97*(7), 471–489. https://doi.org/10.1175/1520-0493(1969)097<0471:mopct>2.3.co;2

Sofiev, M., Ermakova, T., & Vankevich, R. (2012). Evaluation of the smoke-injection height from wild-land fires using remote-sensing data. *Atmospheric Chemistry and Physics*, *12*(4), 1995–2006. https://doi.org/10.5194/acp-12-1995-2012

Sofiev, M., Vankevich, R., Ermakova, T., & Hakkarainen, J. (2013). Global mapping of maximum emission heights and resulting vertical profiles of wildfire emissions. *Atmospheric Chemistry and Physics*, *13*(14), 7039–7052. https://doi.org/10.5194/acp-13-7039-2013

Stein, A. F., Rolph, G. D., Draxler, R. R., Stunder, B., & Ruminski, M. (2009). Verification of the NOAA smoke forecasting system: Model sensitivity to the injection height. *Weather and Forecasting*, *24*(2), 379–394. https://doi.org/10.1175/2008waf2222166.1

Tackett, J. L., Winker, D. M., Getzewich, B. J., Vaughan, M. A., Young, S. A., & Kar, J. (2018). CALIPSO lidar level 3 aerosol profile product: Version 3 algorithm design. *Atmospheric Measurement Techniques*, *11*(7), 4129–4152. https://doi.org/10.5194/amt-11-4129-2018

Teutschbein, C., & Seibert, J. (2012). Bias correction of regional climate model simulations for hydrological climate-change impact studies: Review and evaluation of different methods. *Journal of Hydrology*, *456–457*(457), 12–29. https://doi.org/10.1016/j.jhydrol.2012.05.052

Tosca, M. G., Diner, D. J., Garay, M. J., & Kalashnikova, O. V. (2015). Human-caused fires limit convection in tropical Africa: First temporal observations and attribution. *Geophysical Research Letters*, *42*, 6492–6501. https://doi.org/10.1002/2015GL065063

Tosca, M. G., Randerson, J. T., & Zender, C. S. (2013). Global impact of smoke aerosols from landscape fires on climate and the Hadley circulation. *Atmospheric Chemistry and Physics*, *13*(10), 5227–5241. https://doi.org/10.5194/acp-13-5227-2013

Tosca, M. G., Randerson, J. T., Zender, C. S., Nelson, D. L., Diner, D. J., & Logan, J. A. (2011). Dynamics of fire plumes and smoke clouds associated with peat and deforestation fires in Indonesia. *Journal of Geophysical Research*, *116*, D08207. https://doi.org/10.1029/2010JD015148

Trentmann, J., Andreae, M. O., Graf, H.-F., Hobbs, P. V. V., Ottmar, R. D. D., & Trautmann, T. (2002). Simulation of a biomass-burning plume: Comparison of model results with observations. *Journal of Geophysical Research*, *107*(D2), 4013. https://doi.org/10.1029/2001JD000410

Turner, J. S. (1979). *Buoyancy effects in fluids*. Cambridge, UK: Cambridge University Press.

Val Martin, M., Kahn, R., & Tosca, M. (2018). A global analysis of wildfire smoke injection heights derived from space-based multi-angle imaging. *Remote Sensing*, *10*(10), 1609. https://doi.org/10.3390/rs10101609

Val Martin, M., Kahn, R. A., Logan, J. A., Paugam, R., Wooster, M., & Ichoku, C. (2012). Space-based observational constraints for 1-D fire smoke plume-rise models. *Journal of Geophysical Research*, *117*, D22204. https://doi.org/10.1029/2012JD018370

Val Martin, M., Logan, J. A., Kahn, D., Leung, F. Y., Nelson, D., & Diner, D. (2010). Smoke injection heights from fires in North America: Analysis of 5 years of satellite observations. *Atmospheric Chemistry and Physics Discussions*, *9*(5), 20515–20566. https://doi.org/10.5194/acpd-9-20515-2009

van der Werf, G. R., Randerson, J. T., Giglio, L., Collatz, G. J., Kasibhatla, P. S., & Arellano, A. F. (2006). Interannual variability in global biomass burning emissions from 1997 to 2004. *Atmospheric Chemistry and Physics*, *6*(11), 3423–3441. https://doi.org/10.5194/acp-6-3423-2006

Veira, A., Kloster, S., Schutgens, N. A. J., & Kaiser, J. W. (2015). Fire emission heights in the climate system—Part 2: Impact on transport, black carbon concentrations and radiation. *Atmospheric Chemistry and Physics*, *15*(13), 7173–7193. https://doi.org/10.5194/acp-15-7173-2015

Veira, A., Kloster, S., Wilkenskjeld, S., & Remy, S. (2015). Fire emission heights in the climate system—Part 1: Global plume height patterns simulated by ECHAM6-HAM2. *Atmospheric Chemistry and Physics*, *15*. https://doi.org/10.5194/acp-15-7155-2015

Vermote, E., Ellicott, E., Dubovik, O., Lapyonok, T., Chin, M., Giglio, L., & Roberts, G. J. (2009). An approach to estimate global biomass burning emissions of organic and black carbon from MODIS fire radiative power. *Journal of Geophysical Research*, *114*, D18205. https://doi.org/10.1029/2008JD011188

Vernon, C. J., Bolt, R., Canty, T., & Kahn, R. A. (2018). The impact of MISR-derived injection height initialization on wildfire and volcanic plume dispersion in the HYSPLIT model. *Atmospheric Measurement Techniques*, *11*, 6289–6307. https://doi.org/10.5194/amt-11-6289-2018

Winiger, P., Andersson, A., Eckhardt, S., Stohl, A., & Gustafsson, Ö. (2016). The sources of atmospheric black carbon at a European gateway to the Arctic. *Nature Communications*, *7*, 12776. https://doi.org/10.1038/ncomms12776

Winker, D. M., Pelon, J., Coakley, J. A., Ackerman, S. A., Charlson, R. J., Colarco, P. R., et al. (2010). The CALIPSO mission. *Bulletin of the American Meteorological Society*, *91*(9), 1211–1230. https://doi.org/10.1175/2010bams3009.1

Wooster, M. J., Roberts, G., Perry, G. L. W., & Kaufman, Y. J. (2005). Retrieval of biomass combustion rates and totals from fire radiative power observations: FRP derivation and calibration relationships between biomass consumption and fire radiative energy release. *Journal of Geophysical Research*, *110*, D24311. https://doi.org/10.1029/2005JD006318

Wooster, M. J., & Zhang, Y. H. (2004). Boreal forest fires burn less intensely in Russia than in North America. *Geophysical Research Letters*, *31*, L20505. https://doi.org/10.1029/2004GL020805

Wu, M., Liu, X., Yu, H., Wang, H., Shi, Y., Yang, K., et al. (2020). *Understanding processes that control dust spatial distributions with global climate models and satellite observations (preprint). Aerosols/atmospheric modelling/troposphere/physics (physical properties and processes)*. https://doi.org/10.5194/acp-2020-160

Yanai, M., Esbensen, S., & Chu, J.-H. (1973). Determination of bulk properties of tropical cloud clusters from large-scale heat and moisture budgets. *Journal of the Atmospheric Sciences*, *30*(4), 611–627. https://doi.org/10.1175/1520-0469(1973)030<0611:dobpot>2.0.co;2

Yu, P., Toon, O. B., Bardeen, C. G., Zhu, Y., Rosenlof, K. H., Portmann, R. W., et al. (2019). Black carbon lofts wildfire smoke high into the stratosphere to form a persistent plume. *Science*, *590*, 587–590. https://doi.org/10.1126/science.aax1748

Zeng, T., Wang, Y., Yoshida, Y., Tian, D., Russell, A. G., & Barnard, W. R. (2008). Impacts of prescribed fires on air quality over the Southeastern United States in spring based on modeling and ground/satellite measurements. *Environmental Science and Technology*, *42*(22), 8401–8406. https://doi.org/10.1021/es800363d

Zhang, A., Wang, Y., Zhang, Y., Weber, R. J., Song, Y., Ke, Z., & Zou, Y. (2020). Modeling global radiative effect of brown carbon: A larger heating source in the tropical free troposphere than black carbon. *Atmospheric Chemistry and Physics Discussions*, 1–36. https://doi.org/10.5194/acp-2019-594

Zhu, L., Val Martin, M., Gatti, L. V., Kahn, R., Hecobian, A., & Fischer, E. V. (2018). Development and implementation of a new biomass burning emissions injection height scheme (BBEIH v1.0) for the GEOS-Chem model (v9-01-01). *Geoscientific Model Development*, *11*(10), 4103–4116. https://doi.org/10.5194/gmd-11-4103-2018

Zou, Y., Wang, Y., Ke, Z., Tian, H., Yang, J., & Liu, Y. (2019). Development of a REgion-Specific Ecosystem Feedback Fire (RESFire) model in the Community Earth System Model. *Journal of Advances in Modeling Earth Systems*, *11*, 417–445. https://doi.org/10.1029/2018MS001368